Journal of Materials Chemistry A

ROYAL SOCIETY OF CHEMISTRY

PAPER

View Article Online
View Journal | View Issue

Cite this: J. Mater. Chem. A, 2023, 11, 408

Effective defect passivation with a designer ionic molecule for high-efficiency vapour-deposited inorganic phase-pure $CsPbBr_3$ perovskite solar cells†

Ruxin Guo, ‡[ad] Junmin Xia,‡[b] Hao Gu,‡[b] Xuke Chu,[a] Yan Zhao,[a] Xianghuan Meng,[a] Zhiheng Wu,[ad] Jiangning Li,[a] Yanyan Duan,[a] Zhenzhen Li,[a] Zhaorui Wen,[b] Shi Chen,[b] Yongqing Cai,[b] Chao Liang,*[c] Yonglong Shen,*[ad] Guichuan Xing,*[b] Wei Zhang[e] and Guosheng Shao*[ad]

While caesium lead bromide ($CsPbBr_3$) is promising for highly stable perovskite solar cells (PSCs), the usual solution-based methods require tedious multistep spin coating processes, which imposes a practical barrier against scaling up to large areas for industrial exploitation. Although sequential vapour deposition (SVD) can meet commercial requirements, these films are limited by high trap density and impure phases, resulting in poor performance of PSCs. Here, we obtained low-trap density and effectively phase-pure $CsPbBr_3$ films (grain size > 3 μm, trap density < 4×10^{15} cm^{-3}) by systematic defect and phase management. With the identification of a molecular ionic liquid from theoretical simulation, we find that such a designer molecule can form multiple bonding interactions with the perovskite phase. This results in significantly enhanced crystallization of the $CsPbBr_3$ phase, and more importantly, effective passivation of well recognized Cs- and Br-vacancy defects. $CsPbBr_3$ PSCs with simplified architecture using carbon as electrodes without hole transport layer (HTL) achieved highest power conversion efficiency (PCE) of up to 11.21% for small area devices (0.04 cm^2) and 9.18% for large area devices (1 cm^2). The unencapsulated devices exhibited excellent long-term stability, maintaining over 91% of the initial PCE after 100 days in ambient air at a humidity of ~55%. This work also provides a valuable approach to process phase-pure, low-defect, and large-area inorganic $CsPbBr_3$ perovskite films for efficient and stable optoelectronic devices.

Received 1st August 2022
Accepted 5th November 2022

DOI: 10.1039/d2ta06092b

rsc.li/materials-a

Introduction

The power conversion efficiency (PCE) of organic–inorganic hybrid perovskite solar cells (PSCs) has rapidly increased from 3.8% in 2009 to the latest certified 25.7%, which is comparable to that of silicon-based solar cells.[1,2] However, the organic components in the perovskite layer, hygroscopic additives on the hole transport layer (HTL), and the use of precious metal electrodes have resulted in poor humidity and thermal instabilities as well as high cost of the organic–inorganic hybrid PSCs, which has severely hindered their application in the photovoltaic industry.[3] Carbon-based HTL-free PSCs (C-PSCs) with an all-inorganic caesium lead bromide ($CsPbBr_3$) as the light absorber is currently considered as a most promising approach to overcome the above-mentioned limitations, owing to the substitution of unstable organic cations with inorganic caesium ones and the replacement of organic HTLs as well as precious metal electrodes with low-cost carbon.[4]

In 2016, a $CsPbBr_3$ C-PSC with a PCE of 6.7% was first reported by Liang *et al.*, which has attracted widespread attention because of its excellent environmental stability.[5] For example, Duan *et al.* introduced Ln^{3+} ions into $CsPbBr_3$ to increase the grain size, thereby prolonging the carrier lifetime and increasing the PCEs of photovoltaic devices to 10.14%.[6]

[a]State Centre for International Cooperation on Designer Low-carbon & Environmental Materials (CDLCEM), School of Materials Science and Engineering, Zhengzhou University, Zhengzhou 450001, P. R. China. E-mail: shenyonglong@zzu.edu.cn; gsshao@zzu.edu.cn

[b]Joint Key Laboratory of the Ministry of Education, Institute of Applied Physics and Materials Engineering, University of Macau, Avenida da Universidade, Taipa, Macau 999078, P. R. China. E-mail: gcxing@um.edu.mo

[c]MOE Key Laboratory for Nonequilibrium Synthesis and Modulation of Condensed Matter, School of Physics, Xi'an Jiaotong University, Xi'an 710049, P. R. China. E-mail: chaoliang@um.edu.mo

[d]Zhengzhou Materials Genome Institute (ZMGI), Building 2, Zhongyuanzhigu, Xingyang, Zhengzhou 450100, P. R. China

[e]Advanced Technology Institute (ATI), University of Surrey, Guildford, Surrey, GU27XH, UK

† Electronic supplementary information (ESI) available. See DOI: https://doi.org/10.1039/d2ta06092b

‡ The authors contributed equally.

Subsequently, the PCEs of the state-of-the-art $CsPbBr_3$ C-PSCs further increased to 11.08% with a high open-circuit voltage (V_{oc}) of 1.702 V by incorporating a 2D Cl-terminated Ti_3C_2 ($Ti_3C_2Cl_x$) MXene into the bulk and surface of $CsPbBr_3$ films.[7] However, because of the low solubility of caesium bromide (CsBr), the $CsPbBr_3$ film can only be prepared by a tedious multistep spin coating for the solution process, which is not conducive to industrial application in the future.[7,8] Thus, vapour deposition has been utilized to achieve large-area perovskite films, which has been demonstrated to be the most prospective method for commercial optoelectronic thin-film devices.[8–10] Unfortunately, $CsPbBr_3$ films prepared by vapour deposition usually involve impurity phases of Cs_4PbBr_6 and $CsPb_2Br_5$, which not only introduces defects but also accelerates the decomposition of the films, thereby reducing the performance of PSCs.[8,11] Although substantial efforts have been made in development of processing technology and interface engineering, the fabrication of low-defect and phase-pure $CsPbBr_3$ films remains a bottleneck, hindering further development of the $CsPbBr_3$ PSCs.

As demonstrated in our recent work, strong ionic coordination between ionic liquids (ILs) and the perovskite framework can induce the formation of phase-pure hybrid perovskite films.[12] In addition, the incorporation of ILs into perovskite films significantly improves the performance and long-term stability of the devices, owing to defect passivation and suppression of compositional segregation.[13–17] Herein, we have identified a novel 4-(dimethylamino)-1-(2,2,2-trifluoroacetyl) pyridin-1-ium 2,2,2-trifluoroacetate (DTPT) IL to achieve phase-pure $CsPbBr_3$ films. X-ray diffraction (XRD), high-resolution transmission electron microscopy (HRTEM), and spectroscopic characterizations were used to evaluate the results. In addition, both simulations and experiments indicated that amino, acetyl, and acetate functional groups in DTPT comprehensively passivated the defects in the perovskite crystals, Cs (V_{Cs}) and Br (V_{Br}) vacancies, effectively suppressing non-radiative recombination. As a result, the PSCs based on the device structure of FTO/TiO_2/DTPT/$CsPbBr_3$/DTPT/Carbon achieved a PCE of 11.21% for active area of 0.04 cm^2, which is the highest efficiency reported for $CsPbBr_3$-based PSCs. More importantly, we achieved a PCE of 9.18% for the device with an active area of 1 cm^2, representing the most efficient large-area $CsPbBr_3$-based PSCs. Furthermore, the optimized device retained ~91% of its initial PCE in ambient air at a relative humidity (RH) of ~55%, owing to the high-quality $CsPbBr_3$ films and hydrophobic trifluoro (CF_3–) groups in DTPT.

Results and discussion

The design of ILs play a key role in the defects and phase management of perovskite films. As shown in Fig. 1a, DTPT was designed as an ingenious interface layer owing to the comprehensive functional groups, including pyridine, amino, acetyl, acetate, and CF_3–. In addition, a typical carbon-based HTL-free structure with FTO/TiO_2/DTPT/$CsPbBr_3$/DTPT/Carbon was employed in this study. It is well known that the electron transporting layer (ETL) is crucial for perovskite films and devices due to its surface morphology and roughness.[18–20] Therefore, we first investigated the influence of DTPT modification on the TiO_2 ETL, as shown in ESI, Fig. S1 and S2.† When the DTPT molecule was assembled onto the surface of a TiO_2 film, root-mean-squared (RMS) roughness decreased from 36.5 to 27.8 nm. Additionally, owing to the existence of the hydrophobic CF_3– functional group, the contact angle was enhanced on the TiO_2 surface after DTPT modification (ESI, Fig. S3†), which could have decreased the hetero-nucleation of perovskite, thereby increasing the grain size of the $CsPbBr_3$ phase in the film (ESI, Fig. S4†).[21] Notably, the number of XRD diffraction peaks of Cs_4PbBr_6 in the $CsPbBr_3$ film were markedly reduced from four down to one albeit without enhancement of the intensity of the only remnant peak of (321) plane (ESI, Fig. S5†), indicating that the phase purity of the $CsPbBr_3$ film with DTPT on TiO_2 substrate was effectively improved owing to suppressed nucleation of the impurity phases. The photovoltaic performance of PSCs based on TiO_2 and TiO_2/DTPT is shown in ESI, Fig. S6 and S7.† The current density–voltage (J–V) curves of PSCs based on TiO_2 and TiO_2/DTPT are shown in ESI, Fig. S6a,† and the corresponding photovoltaic performance data are summarized in ESI, Table S1.† Compared to the untreated, the device based on TiO_2/DTPT has increased short-circuit current density (J_{sc}) from 8.22 mA cm^{-2} to 8.43 mA cm^{-2}, V_{oc} from 1.521 V to 1.535 V, FF from 78.66% to 79.87%, and PCE from 9.83% to 10.34%. The significant enhancement of J_{sc} and decrease of the hysteresis (ESI, Fig. S7†) may be attributed to the smooth surface of TiO_2/DTPT, which is conducive to $CsPbBr_3$ large grain growth and charge transport collection efficiency.[21] As shown in ESI, Fig. S8,† the $CsPbBr_3$ layer under the treated film has a high light absorption, which ensures more sunlight to be utilized by the $CsPbBr_3$ layer for achieving high PCE.[6] In addition, to demonstrate the reproducibility of PSCs based on TiO_2 and TiO_2/DTPT, the PCE distribution histogram (40 individual devices) is shown in ESI, Fig. S6b.† The result demonstrates that the efficiency of PSCs prepared based on TiO_2/DTPT shows a narrower distribution, and the high-quality uniform growth of perovskite films may be the reason for the good reproducibility of the devices.[8]

DTPT was then applied to treat the above $CsPbBr_3$ film, (TiO_2/DTFT/)$CsPbBr_3$/DTFT. The XRD patterns of $CsPbBr_3$ and $CsPbBr_3$/DTPT are shown in Fig. 1b. All of the peaks at 15.2°, 21.5°, 26.4°, 30.7°, and 37.8° correspond to the (100), (110), (111), (200), and (−121) crystal planes of the phase of $CsPbBr_3$ (PDF#18-0364), respectively. However, the diffraction peak for the (321) plane of the Cs_4PbBr_6 phase (PDF#73-2478) was not evident.

HRTEM and selected area electron diffraction (SAED) were used to investigate the effect of DTPT on the perovskite structure, as shown in Fig. 1c and ESI, Fig. S9–S11.† The lattice spacing of 0.413 nm in Fig. 1c corresponds to the (110) plane in the $CsPbBr_3$ phase in the crystal direction of [1−1−1], which is consistent with the diffraction peak in the XRD pattern. The enhanced peak intensity for the (110) plane in the XRD pattern indicates the preferred orientation along its normal vector. As shown in ESI, Fig. S9,† the SAED pattern of the $CsPbBr_3$/DTPT films is typically single crystalline, indicating no sub-grain

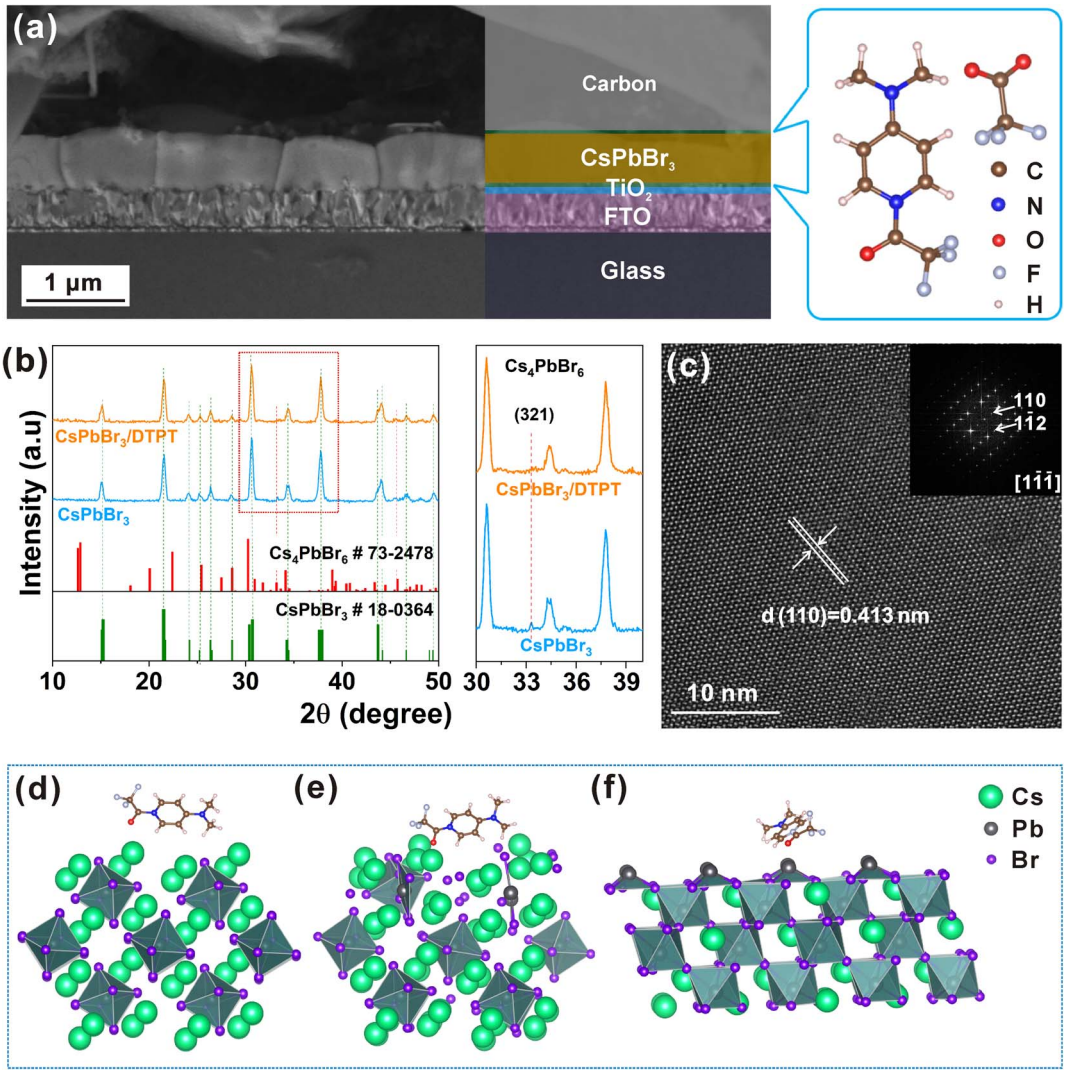

Fig. 1 (a) Cross-sectional SEM image of $CsPbBr_3$ PSC and chemical structure of the ionic liquid DTPT. (b) XRD patterns and Cs_4PbBr_6 for (321) planes of the $CsPbBr_3$ and $CsPbBr_3$/DTPT films. (c) HRTEM and FFT of the $CsPbBr_3$/DTPT film. The structures of the Cs_4PbBr_6 with DTPT on the surface (d) before optimization and (e) after optimization. (f) The (110) phase structure of $CsPbBr_3$ with DTPT on the surface.

boundaries within each fairly large crystal in the over micrometre grains. The SAED pattern (selected from the region shown in ESI, Fig. S9a†) of the $CsPbBr_3$/DTPT films was used to demonstrate that the DTPT-modified $CsPbBr_3$ film has a single orientation over a large range. In contrast, the Cs_4PbBr_6 phase was observed in the $CsPbBr_3$ film without DTPT treatment (ESI, Fig. S10†). The lattice spacing of 0.269 nm corresponds to the (321) plane of the Cs_4PbBr_6 phase, which is consistent with the XRD results. Meanwhile, a small amount of $PbBr_2$ phase exists in the $CsPbBr_3$ film without DTPT treatment (ESI, Fig. S11†). Overall, the TEM results agree well with the XRD outcome, in that the impurity phases were only present in the sample without the top-surface DTPT treatment, but treatment with DTPT of the perovskite film helped eliminate $PbBr_2$/Cs_4PbBr_6 impurities. Such DTPT effect is similar to previous finding that the presence of pyridine lowers the activation energy for the transformation of $PbBr_2$/Cs_4PbBr_6 into the $CsPbBr_3$ phase.[22] The promoted phase purity is essential to benefit the performance and stability of perovskite PV cells.[23]

To further elaborate the possibility of the phase transition process from Cs_4PbBr_6 to $CsPbBr_3$ by DTPT, we conducted density functional theory (DFT) simulation. The Cs_4PbBr_6 phase was found to be relatively stable when it was not modified by DTPT. The modifying molecule (Fig. 1d) will interact with the surface of the Cs_4PbBr_6 phase, resulting in local structural damage to the Cs_4PbBr_6. As shown in Fig. 1e, as the octahedron $PbBr_6^{4-}$ structure on the surface of the Cs_4PbBr_6 phase was undermined, it tends to restructure with neighbouring species to form the $CsPbBr_3$ phase. Such a catalytic effect is to help facilitate reaction with nearby $PbBr_2$, while the lower-nanoscale structures of impurity phases provide further leverage to enable such reaction at a moderate temperature during the after-treatment heating at 373 K.

In addition, we confirmed the preferred crystal orientation with modified molecules in the $CsPbBr_3$ phase *via* simulation.

In the presence of DTPT, it was found that the (110) plane had a lower formation energy than the (001) plane, −0.504 eV and −0.067 eV, respectively, as shown in Fig. 1f and ESI, Fig. S12.† This indicates that the DTPT molecule can promote the formation of the (110) plane as a higher orientation of $CsPbBr_3$ than the (001) plane, which is consistent with the XRD and HRTEM results. From the enlarged XRD spectra of $CsPbBr_3$ films deposited on TiO_2 and TiO_2/DTPT films in ESI, Fig. S13a,† it can be seen that the diffraction peak of the (110) plane of the $CsPbBr_3$ film is significantly enhanced after DTPT modification of the TiO_2 surface. However, as shown in ESI, Fig. S13b,† the diffraction peak of (110) plane before and after the DTPT modification of $CsPbBr_3$ surface is not obvious (ESI, Fig. S13c†), since the prior DTPT treatment of the TiO_2 substrate already delivered such an orientational benefit (Fig. S13a and c†), with the crystallization of Cs_4PbBr_6 phase largely prevented.

To investigate the surface chemical states of DTPT on the $CsPbBr_3$ film, we conducted X-ray photoelectron spectroscopy (XPS). The high-resolution XPS spectra of Cs 3d, Pb 4f, Br 3d, and F 1s are presented in Fig. 2a–d, respectively. In pristine $CsPbBr_3$ films, the binding energies of 724.34 and 738.27 eV correspond to the Cs $3d_{5/2}$ and Cs $3d_{3/2}$ peaks, respectively. After DTPT modification, the two typical peaks shifted to 724.58 and 738.51 eV, respectively, which may be attributed to the strong coupling effect between the Cs^+ vacancies and amino functional group in DTPT.[24] In addition, the 0.31 and 0.28 eV upshift of Pb 4f and Br 3d peaks, respectively, may be associated with the strengthened interaction between the O atom in the acetyl/acetate functional group and Pb species (or Br^- vacancies). As expected, we also detected the F 1s peak at 688.28 eV in the DTPT-modified sample, which is consistent with the time-of-flight secondary-ion mass spectrometry (ToF-SIMS) results (ESI, Fig. S14†).[16]

To further elaborate the DTPT interactions with defects, we conducted DFT modelling on the most common ionic defects of Cs vacancies (V_{Cs}) and Br vacancies (V_{Br}) in $CsPbBr_3$.[25] The ESI, Fig. S15† depicts the structures of $CsPbBr_3$ with various vacancies and DTPT. Generally, the density of states (DOS) provides an intuitive description of the passivation effect. As shown in Fig. 2e, V_{Cs} caused the Fermi level to insert into the top of the valence band (VB) and bring an obvious trap state, which suppressed the separation of charge carriers and formed recombination centers.[26] When the DTPT was anchored on the V_{Cs} site, we found that the Fermi level had a distinct blue shift and returned to the bandgap. Furthermore, the trap state at the VB was remarkably reduced, which was also evidenced by the

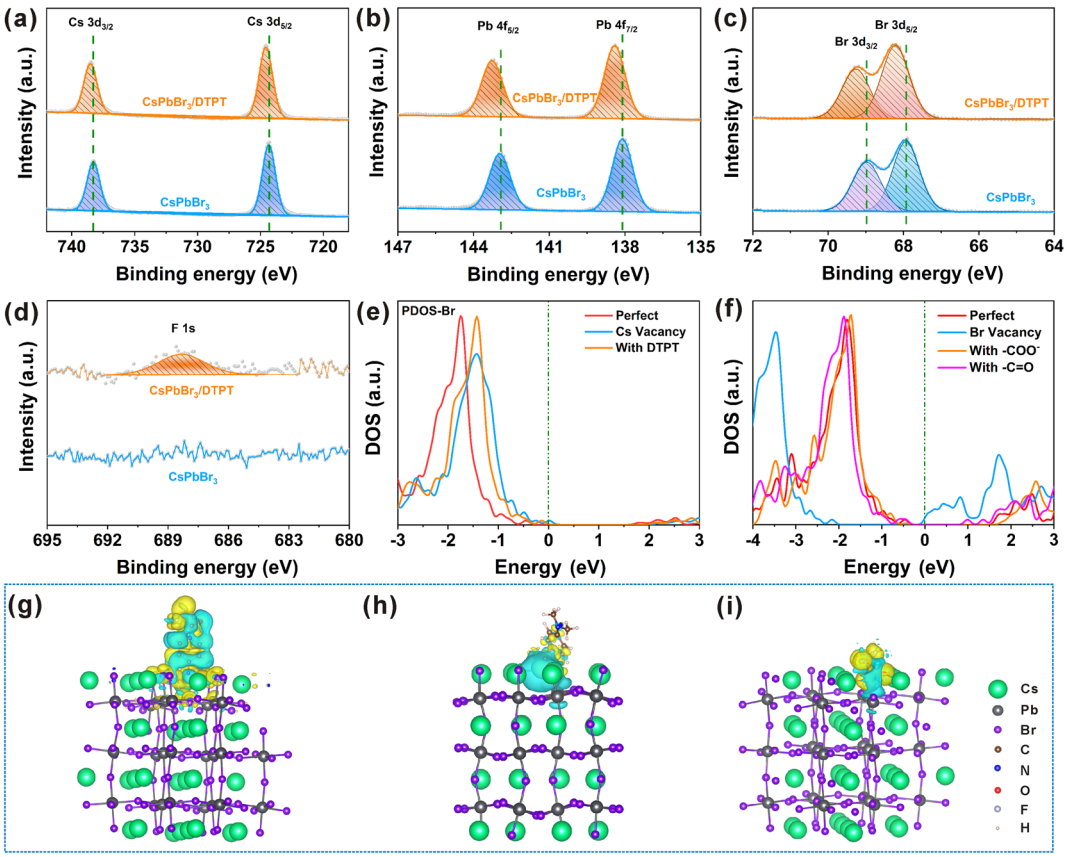

Fig. 2 High-resolution XPS analysis of (a) Cs 3d, (b) Pb 4f, (c) Br 3d, and (d) F 1s in $CsPbBr_3$ and $CsPbBr_3$/DTPT films. (e) Electronic partial density of state (PDOS) curves for Br of the $CsPbBr_3$ with V_{Cs} passivated by DTPT. (f) Density of state (DOS) of $CsPbBr_3$ with V_{Br} passivated by the carboxylic acid group in CF_3COO^- and the C=O in DTPT. The Fermi level (represented by a dashed line) has been set to zero. Differential charge density when DTPT fills into the vacancies of $CsPbBr_3$. (g) V_{Cs} passivated by the DTPT; V_{Br} passivated by (h) the C=O in DTPT and (i) the carboxylic acid group in CF_3COO^-. The blue (yellow) isosurfaces represent the dissipation (accumulation) of electron density.

electron localization function (ELF) results. As shown in ESI, Fig. S16,† the profile of ELF around V_{Cs} is similar to that of the perfect $CsPbBr_3$ structure obtained after introducing DTPT, which indicated that the grafted amino functional group could imitate the role of Cs atoms to mitigate the delocalization of the wave function around Br ions caused by V_{Cs}.[27] To further explore the mechanism, we calculated the differential charge density (DCD) of the system.[16] Fundamentally, the passivation molecule had an apparent interaction with the peripheral atoms around the V_{CS}, implying that DTPT can effectively modulate the defective structure.

For V_{Br}, as both acetyl/acetate and CF_3– functional groups may coordinate with the exposed Pb atoms, we investigated the adsorption configurations of the molecules with different sites.[28] First, we calculated the adsorption energies of the different systems to predict the appropriate passivation methods using the following eqn (1):

$$E_{ad} = E_{molecule/CsPbBr_3} - E_{molecule} - E_{CsPbBr_3} \quad (1)$$

where E_{ad} indicates the adsorption energy of the molecules on the surface and the negative E_{ad} represents a molecule that can be stably adsorbed on the surface. $E_{molecule/CsPbBr_3}$, $E_{molecule}$, and E_{CsPbBr_3} represent the total energies of the passivated systems, passivation molecule, and $CsPbBr_3$ with V_{Br}, respectively. We found that the acetyl/acetate group is suitable for coordinating with Pb species as the adsorption energy was lower than that of the coordinated CF_3– group. As shown in the ELF (ESI, Fig. S16†), V_{Br} promotes the deformation of electron localization surrounding the lead atoms, which leads to non-radiative events. In contrast, when the acetyl/acetate group of DTPT adsorbs above the Pb ion, the state reverts to defect-free parts because of the passivation of the dangling states of the uncoordinated Pb atoms. The DOS of the passivated systems indicates that both the acetyl and acetate groups of DTPT have a remarkable passivation effect on the V_{Br}. As shown in Fig. 2f, the Fermi level is located at the conduction band (CB) with the V_{Br}, while it returned to the bandgap after passivation. More importantly, when we focused on the density state of the Pb atom around the V_{Br}, the trap state was found to be remarkably reduced (ESI, Fig. S18a†). Meanwhile, because of the suppression of electron localizations surrounding the lead atoms, the peak of the trap state at the edge of CB exhibited a distinct blue shift after the DTPT was absorbed, accounting for the prolonged lifetime of excited electrons and indicating the inhibition of the unfruitful recombination in the devices.[29] Furthermore, the DCD distributions of the systems, shown in Fig. 2h and i, suggest that electrons are transferred from the $CsPbBr_3$ (with V_{Br}) to the adsorbed DTPT groups. This is consistent with the XPS results, in which all atoms, including Cs, Pb, and Br, suffered electron loss.[30] Similarly, we also determined the state of the passivated CF_3– group. As shown in ESI, Fig. S17,† the results of both DCD and ELF indicate that the CF_3– group has an effect like that of the acetyl/acetate group on DTPT. However, the DOS (ESI, Fig. S18b†) shows that the CF_3– group on the cationic part could not provide the expected passivation effect. Therefore, the CF_3– functional group mainly contributed to the improvement in stability. In addition, C=O in DTPT (−2.03 eV) has a lower formation energy when passivating Br defects than CF_3– group (−1.65 eV) in DTPT, so C=O has a stronger interaction with surface with Br vacancy. Overall, DTPT has a comprehensive passivation effect on the $CsPbBr_3$ films based on amino, acetyl, and acetate functional groups, which modulate the defective structures.[31]

To explore the photophysical mechanisms involved in the enhancement of DTPT modified devices, we used temperature-dependent photoluminescence (PL), time-resolved PL (TRPL), and femtosecond transient absorption (fs-TA) measurements. First, the temperature-dependent PL was conducted from 40 to 300 K for the $CsPbBr_3$ and $CsPbBr_3$/DTPT films, as shown in Fig. 3a and b, which indicated that the fluorescence intensity decreased with increasing temperature due to temperature-activated exciton dissociation.[32,33] Notably, there was a significant red shift in the PL peak position after DTPT modification, which is related to the reduced quantum confinement in the phase-pure $CsPbBr_3$ films.[34] In addition, the PL spectrum of the $CsPbBr_3$ film modified by DTPT indicated a narrower full width at half maximum (FWHM), further indicating that the DTPT modification can effectively reduce shallow- or deep-level defects and eliminate the Cs_4PbBr_6 phase.[35] The exciton binding energy (E_b) is an important parameter for photovoltaic materials, which represents the energy required for the separation of bound excitons into free carriers. As shown in Fig. 3c, E_b can be obtained by fitting the relationship between the integrated PL intensity and temperature using the following Arrhenius equation:

$$I(T) = \frac{I_0}{1 + Ae^{-E_b/k_B T}} \quad (2)$$

where I_0 is the integrated PL intensity at 0 K and K_B is the Boltzmann constant.[36,37] The E_b of $CsPbBr_3$ before and after modification was 123 ± 10 and 94 ± 9 meV, respectively, which is consistent with a previous report.[38] The reduced E_b can improve the exciton dissociation efficiency, thus reducing carrier recombination and ultimately increasing the device performance.[35] Furthermore, we used a previously developed theoretical model of photo-injected carrier density-dependent integrated PL intensity to estimate the trap density of the control and $CsPbBr_3$/DTPT films. Generally, the low and high photo-injected carrier densities correspond to the non-radiative recombination in the low-lying traps and the radiative recombination after the traps are filled, respectively.[39,40] The relationship between the integrated PL intensity and photo-injected carrier density is shown in Fig. 3d, and the fitting curve shows that the trap density of the $CsPbBr_3$ film reduced from 1.5×10^{16} to 3.1×10^{15} cm^{-3} after the DTPT treatment. As shown in Fig. 3e, TRPL decay was used to investigate the effect of DTPT on the carrier lifetime of the perovskite films. The perovskite film modified with DTPT had a longer carrier lifetime (27 ns) than that of the untreated perovskite film (4.5 ns). This was because of the suppression of non-radiative recombination, which accelerated charge extraction and transfer, enhancing the performance and reduction of *J–V* hysteresis in DTPT-modified devices.[41,42] To further study the phase composition and charge

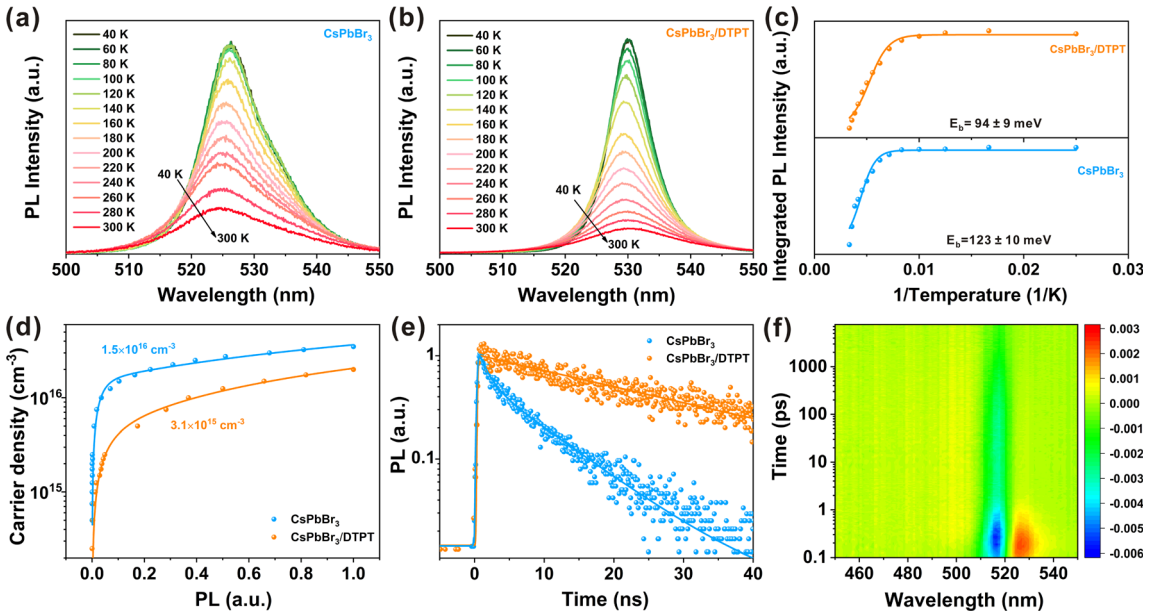

Fig. 3 Temperature-dependent PL spectra of (a) $CsPbBr_3$ and (b) $CsPbBr_3$/DTPT films. (c) Dependence of integrated PL intensity and reciprocal temperature (T^{-1}). (d) The PL intensity *versus* photo-injected carrier density. (e) Time-resolved photoluminescence (TRPL) decay curves of $CsPbBr_3$ and $CsPbBr_3$/DTPT films. (f) Pseudo-colour femtosecond transient absorption (fs-TA) spectrum plots of $CsPbBr_3$/DTPT film upon a pulsed fs-laser excitation at 400 nm.

carrier dynamics in the two perovskite films, fs-TA experiments were conducted under pulsed 400 nm laser excitation (100 fs, 1 kHz, ~1 μJ cm^{-2}). The pseudo-colour fs-TA spectrum of the relative optical density (ΔA) as a function of relaxation time and wavelength (Fig. 3f and ESI, Fig. S19†) indicated that the photobleaching (PB) peak was approximately 518 nm, which is in good agreement with the absorption spectra. Crucially, the $CsPbBr_3$/DTPT sample exhibited a narrower PB signal, indicating that the modified $CsPbBr_3$ perovskite had fewer inherent defects near the band edge than the control.[35] In addition, although the complex biexcitons/charged exciton process (τ_1) was observed in the whole fs-TA dynamics,[43] the modified perovskite film exhibited a single exciton decay time (τ_2) that was six times longer than that of the unmodified $CsPbBr_3$ film (ESI, Fig. S20†). This is consistent with the results of TRPL (Fig. 3e).[42] The results indicated that modifying the surface of the $CsPbBr_3$ film using DTPT can significantly reduce the trap density and optimize the perovskite interface, thereby increasing the performance of the devices.

We conducted light-intensity-dependent J–V measurements and a series of electrochemical tests to profoundly investigate the charge recombination mechanism of the device. The relationship curves of logarithms of J_{sc} and intensity are plotted in Fig. 4a. According to the power law equation: $J_{sc} \propto I^{\alpha}$,[4,17] the factor α related to bimolecular recombination can be calculated, and the value of α is 0.976 for the treated device and 0.959 for the control device, indicating that DTPT treatment can make the carriers transfer from the perovskite layer to the carbon faster and reduce the recombination of the charge at the $CsPbBr_3$/carbon interface.[6,23] Moreover, the factor n related to monomolecular recombination can be obtained by equation: $V_{oc} = nkT\ln(I)/q$ + constant, where k, T and q represent Boltzmann constant, absolute temperature and elementary charge, respectively.[11,17] As shown in Fig. 4b, the n value of the modified device is reduced from 1.67 to 1.38, demonstrating that the DTPT modification of the $CsPbBr_3$ film significantly suppressed the trap assisted recombination process.[7,41] To further evaluate the trap state density (n_{trap}) of the $CsPbBr_3$ films, we performed space charge limited current (SCLC) method under the dark condition. The n_{trap} can be calculated with the trap-filled limit voltage (V_{TFL}) by the equation: $n_{trap} = 2\varepsilon\varepsilon_0 V_{TFL}/qL^2$, where L is the thickness of the perovskite films, ε is the relative dielectric constant of $CsPbBr_3$, ε_0 is the vacuum permittivity, and V_{TFL} is the kink point in the dark I–V curve.[7,44,45] As shown in Fig. 4c, the V_{TFL} is reduced from 1.12 V to 0.67 V after DTPT treatment, we then obtain the n_{trap} of $CsPbBr_3$ and $CsPbBr_3$/DTPT films as 1.54 × 10^{16} cm^{-3} and 9.24 × 10^{15} cm^{-3}, respectively, which is consistent with the results of the previous theoretical model (Fig. 3d). It is proved once again that the treatment of DTPT can effectively passivate the traps in the $CsPbBr_3$ layer, thereby improving the device performance through improved J_{sc} and FF.[41] Besides, the dark J–V curves of devices based on $CsPbBr_3$ and $CsPbBr_3$/DTPT films indicate that the device based on $CsPbBr_3$/DTPT film exhibited a smaller leakage current density under reverse bias in Fig. 4d, which indicates that the DTPT treatment can effectively reduce interface defects and suppress leakage current.[6] To investigate the interfacial charge transfer characteristics of the devices, we performed electrochemical impedance spectroscopy (EIS) measurement at an applied bias of V_{oc} under dark conditions with a frequency range of 0.1 Hz to 100 kHz and an amplitude of 5 mV and fitted with the equivalent circuit shown in the inset in Fig. 4e. The low-frequency arc

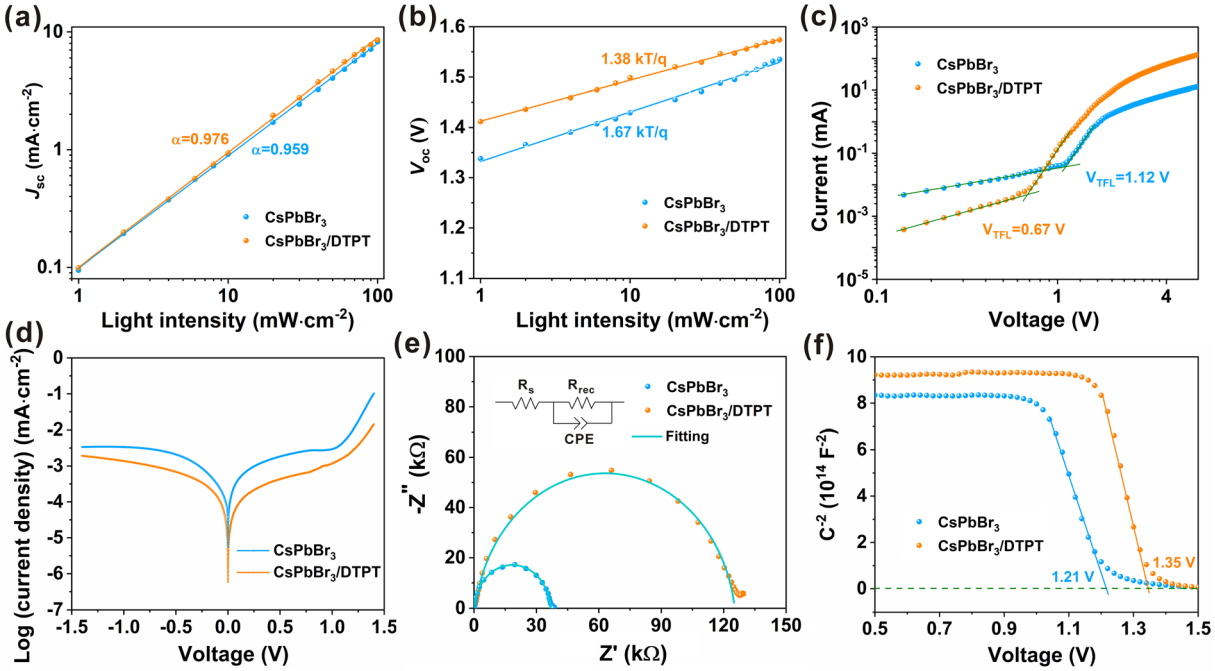

Fig. 4 (a) J_{sc} and (b) V_{oc} dependence on the light intensity. (c) Dark I–V curves with structure of FTO/TiO_2/DTPT/$CsPbBr_3$/PCBM/carbon or FTO/TiO_2/DTPT/$CsPbBr_3$/DTPT/PCBM/carbon. (d) Dark J–V curves, (e) Nyquist plots and the fitting curves, (f) Mott–Schottky (M–S) plots of the devices with and without DTPT.

in the Nyquist plots represents the recombination resistance (R_{rec}) at the interface, and the device after DTPT modification has a larger arc, which means that proper concentration of DTPT to treat the $CsPbBr_3$ surface can effectively inhibit the recombination of interface charges, thereby contributing to enhance J_{sc} and FF of the device.[4,41] Mott–Schottky analysis is often used as a measure to calculate the built-in potential (V_{bi}) of the device, and the equation is $C^{-2} = 2(V_{bi} - V)/\varepsilon_0\varepsilon qA^2N_A$, where C, ε_0, ε, q, A and N_A are the capacitance, vacuum dielectric constant, relative dielectric constant of $CsPbBr_3$, elementary charge, active area of device and carrier concentration, static permittivity, dielectric constant.[7] Therefore, we can obtain V_{bi} from the intercept of the linear region and the x-axis of the reciprocal of the square root of the capacitance and the voltage (C^{-2}–V) curve. As shown in Fig. 4f, DTPT modification increased the V_{bi} from 1.21 to 1.35 V, which is consistent with the increased V_{oc} of the devices. A higher V_{bi} means that the driving force for charge separation is stronger, and the charge accumulation at the perovskite/carbon interface is smaller, resulting in weaker hysteresis behaviour and improved performance. Therefore, modifying the surface of the $CsPbBr_3$ film by DTPT can significantly reduce the energy level mismatch between $CsPbBr_3$ and carbon, thereby increasing the V_{oc} of the PCEs.[4]

To investigate the effect of modifications in DTPT on device performance, we prepared 40 devices for each DTPT concentrations (0–6 mg mL^{-1}), and the results are shown in ESI, Fig. S21.† Optimization revealed that the devices had the highest average PCE (11.14%) and lowest standard deviation (0.061) at 3 mg mL^{-1} of DTPT. We compared the device performance with that of the control and the optimal concentration of DTPT, and the corresponding J–V curve and specific photovoltaic parameters are shown in Fig. 5a and ESI, Table S2.† After modification, the PCE of the devices was significantly enhanced from 10.34% to 11.21% (J_{sc} = 8.52 mA cm^{-2}, V_{oc} = 1.574 V, and fill factor (FF) = 83.67%), which is the best performance reported for all $CsPbBr_3$-based PSCs (ESI, Table S3†).[7,8,11] Notably, the V_{oc} of the devices increased from 1.535 to 1.574 V, possibly due to the reduction of the energy level offset and suppression of non-radiative recombination.[45,46] To prove this hypothesis, ultraviolet photoemission spectroscopy (UPS) measurements (ESI, Fig. S22†) were used to investigate the influence of DTPT modification on the energy level alignment (ESI, Fig. S23†) of the $CsPbBr_3$ films. The cut-off energy ($E_{cut\text{-}off}$) and valence band maximum (VBM) edges of control and modified $CsPbBr_3$ films are shown in ESI, Fig. S22a and b,† where the VBM of $CsPbBr_3$ and $CsPbBr_3$/DTPT are −5.68 and −5.56 eV, respectively. This change in VBM is mainly attributed to a change in the work function, as the change in VBM with reference to the instrumental Fermi level was an order smaller (1.06 *vs.* 1.03 eV, approximately half the band gap value below the instrumental Fermi reference).[23,47] Therefore, the energy offset between the VBM of $CsPbBr_3$ and Fermi level (−5.0 eV) of the carbon electrode decreased from 0.68 to 0.56 eV after the DTPT modification, which corresponded to the improvement in V_{oc} of the devices. The ESI, Fig. S24† displays the J–V curves of PSCs based on $CsPbBr_3$ and $CsPbBr_3$/DTPT under different scanning directions. The hysteresis index (H-index) can be obtained according to the formula: H-index = ($PCE_{Reverse}$ − $PCE_{Forward}$)/$PCE_{Reverse}$, and the H-index of the device with DTPT modification (0.097) was significantly lower

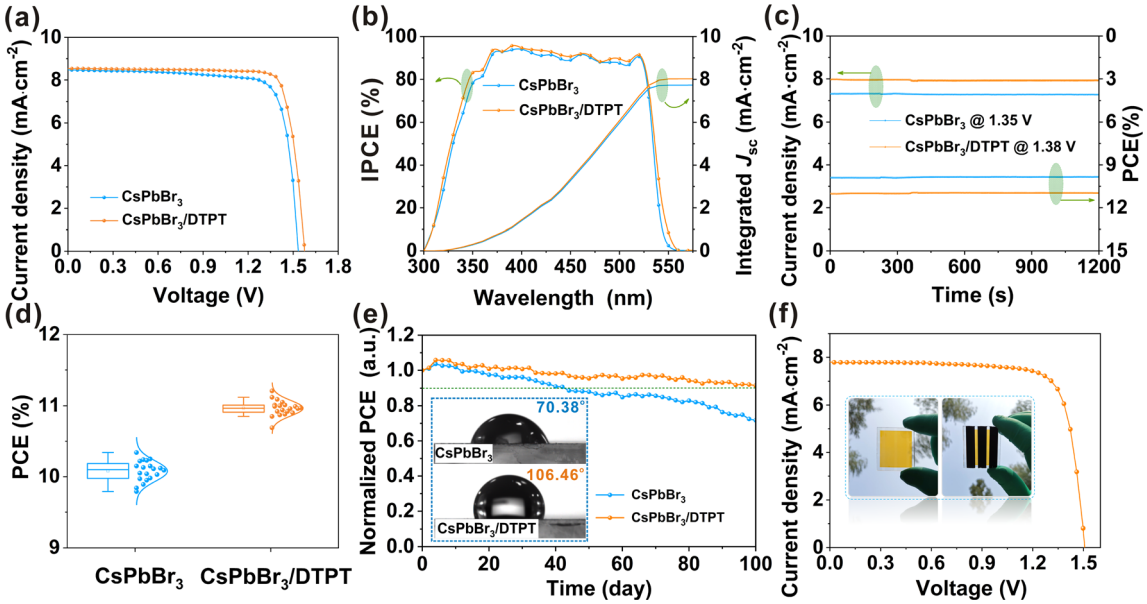

Fig. 5 (a) J–V curves, (b) IPCE spectrum and corresponding integrated current, (c) stabilized power output, (d) PCEs of statistical and (e) long-term stability (~25 °C and ~55% RH) of the devices with and without DTPT; the water contact angle (illustration of (e)) of $CsPbBr_3$ and $CsPbBr_3$/DTPT films, (f) J–V curve of the large area device based on $CsPbBr_3$/DTPT film.

than that of the control device (0.157). We believe that the high FF and low hysteresis are attributed to the low-defect perovskite films and excellent interface of the $CsPbBr_3$/carbon.[45,46]

In addition, the incident photon-to-current efficiency (IPCE) spectrum (Fig. 5b) of the device based on $CsPbBr_3$/DTPT was enhanced over the entire absorption region of 300–550 nm, and the light response edge of the device was slightly red-shifted as compared to that of the control, which agrees with the absorption spectra (ESI, Fig. S25†). As previously reported, the band gap of Cs_4PbBr_6 was ~3.8 eV, which is wider than that of $CsPbBr_3$ (2.3 eV). Thus, the red shift of the photo-response edge occurred due to the presence of DTPT.[48] The integrated current densities obtained using these curves were 7.75 and 8.02 mA·cm^{-2} for the devices based on the control and $CsPbBr_3$/DTPT films, respectively, which are consistent with the J_{sc} values obtained from the J–V curves. The steady-state photocurrent and PCE measured at the maximum power point (MPP) are shown in Fig. 5c. The device modified with DTPT obtained a stable PCE of 11.02%, which is higher than the value of the PCE based on original $CsPbBr_3$ (9.91%), once again verifying the stability and reliability of the modified PSC. Fig. 5d and ESI, Fig. S26† depict the statistical analysis of PCEs, V_{oc}, J_{sc}, and FF for the devices with and without DTPT. The DTPT-modified devices exhibited high reproducibility, which is conducive to large-scale production. In addition, the performance enhancement of modified PSCs is mainly due to the enhancement of V_{oc} and FF, which can be attributed to the optimized energy level alignment, and the reduction of defect-related charge recombination.[4]

The long-term operational stability, a key parameter for PSCs, was also evaluated. Fig. 5e shows the PCE trend of the device placed in an ambient atmosphere of ~25 °C and ~55% RH. After 100 days, the DTPT-modified device exhibited excellent stability and maintained ~91% of its initial performance, while the control device indicated a ~30% reduction in efficiency. The high stability can be attributed to the phase-pure and low-defect $CsPbBr_3$ films.[49–51] In addition, owing to the introduction of the hydrophobic CF_3– functional group in the DTPT molecule, the contact angle increased from 70.38° to 106.46°, which also played a significant role in enhancing the stability of the PSCs (Fig. 5e). Finally, to verify that this strategy can be applied to large-area devices, a device with an active area of 1 cm^2 was prepared. Encouragingly, a PCE of 9.18% was achieved with a V_{oc} of 1.509 V, J_{sc} of 7.81 mA·cm^{-2}, and FF of 77.85% (Fig. 5f), which is also the highest efficiency reported thus far for large-area $CsPbBr_3$-based PSCs (ESI, Table S4†).[23,52]

Experimental

Materials

$PbBr_2$ and CsBr were purchased from the Xi'an Polymer Light Technology Corp. All solutions, carbon paste and 4-(dimethylamino)-1-(2,2,2-trifluoroacetyl)pyridin-1-ium 2,2,2-trifluoroacetate (DTPT) were purchased from Aladdin, the Shanghai MaterWin New Materials Co., Ltd, and TCI respectively.

Device fabrication

Before preparing solar cells, the FTO glasses were cleaned by acetone, ethanol and deionized water for 15 min each and then treated in UV-ozone for 30 min. The treated FTO substrates were soaked in a 200 mM $TiCl_4$ aqueous solution at 70 °C for 1 hour, in which the dilution of the $TiCl_4$ solution (stored in the freezer) needs to be carried out at 0 °C. After washing with deionized

water and ethanol, the substrates were annealed on a heating stage at 100 °C for 1 hour in ambient air.[40] The $CsPbBr_3$ film was fabricated by vapour deposition method, and the film thickness was controlled by a quartz crystal microbalance. Firstly, 100 nm $PbBr_2$ film was deposited on the FTO/TiO_2 substrate, and then removed from the vacuum chamber for 100 °C annealing for 60 min. Then 200 nm CsBr film were deposited on $PbBr_2$ film, and removed from the vacuum chamber for 300 °C annealing for 60 min. Finally, 150 nm $PbBr_2$ film were deposited on CsBr film, and then the $PbBr_2$/CsBr/$PbBr_2$ film was annealed at a heating table at 300 °C for 60 min. Both $PbBr_2$ and CsBr films were deposited under a pressure of $\sim 8.0 \times 10^{-4}$ Pa with a speed of 0.2 Å s^{-1} and all annealing processes were carried out in ambient air. The DTPT was dissolved in isopropyl alcohol with different concentrations and spin-coated on the surface of TiO_2 and $CsPbBr_3$, and then heating at 100 °C in ambient air for 10 min to remove residual solvent. At last, the conductive carbon paste was blade-coated on the $CsPbBr_3$ film and heated at 100 °C for 10 min.

Characterization

The scanning electron microscopy (SEM) images are taken by a field emission SEM (Sigma-500, Zeiss). X-ray diffraction (XRD) was carried out using the Cu Kα radiation (Empyrean, Netherlands). Transmission electron microscopy (TEM) was carried out using a FEI Talos F200X microscope with a field-emission source operating at 200 kV. The current density–voltage (J–V) curves of the devices were performed by using a Keithley 2400 system source meter under AM 1.5G simulated solar illumination. The incident photon-to-electron conversion efficiency (IPCE) was measured using Newport-74125 system (Newport Instrument). X-ray photoelectron spectroscopy (XPS) with Al Kα X-rays (1486.6 eV) and ultraviolet photoelectron spectroscopy (UPS) were performed using AXIS Supra (Kratos, England) under a vacuum of 1×10^{-9} Torr. The XPS spectra was calibrated using the C 1s binding energy of adventitious carbon (AdC) and the sample-work-function (ϕ_{SA}) method by Greczynski and Hultman.[53] The UPS was carried out using the He I ($h\nu = 21.22$ eV), was calibrated with a standard Au film ($\phi = 5.3$ eV) before starting work function measurements.[54] UV-vis-NIR fluorescence spectrophotometer absorption spectra were performed by a Shimadzu UV 3600 spectrophotometer. Steady-state photoluminescence (PL) were tested by self-built fluorescence spectrometer, and the excitation wavelength was 400 nm. TRPL was obtained by an Optronis Optoscope streak camera by using 400 nm pulse laser. The broadband femtosecond TA spectra of the $CsPbBr_3$ films were taken using the Ultrafast System HELIOS TA spectrometer. The 400 nm laser pulses were generated by passing the strong 800 nm femtosecond laser beam through a beta barium borate crystal. All electrochemical tests are performed by the CHI760E electrochemical station of Shanghai Chenhua.

Computational details

DFT calculations are performed using the Vienna *Ab Initio* Simulation Packages (VASP) with the generalized gradient approximation (GGA) proposed by Perdew–Burke–Ernzerhof (PBE).[55] The structure relaxations are carried out with a 450 eV plane-wave cutoff. The Brillouin zone integration was sampled following a gamma-centered Monkhorst–Pack scheme, using $1 \times 1 \times 1$ k-point grids for the ionic optimization and $3 \times 3 \times 3$ k-point grids for the density of state, respectively. The self-consistent total-energy difference and the convergence criterion for forces on atoms are set to 10^{-4} eV and 0.01 eV $Å^{-1}$, respectively. In all of the calculations, the positions of the two atomic layers at the bottom of the slab were kept fixed at the relaxed bulk positions, while the first two layers of the top face, which was the surface under investigation, were fully relaxed. We used a vacuum over 10 Å to adequately separate images along the surface normal direction.

Statistical analysis

Origin software (2018, OriginLab) was used for statistical analysis. Descriptive statistics was performed to evaluate efficiency of different devices, such as the efficiency statistics of devices with and without modification on TiO_2 layer and the efficiency statistics of devices after different concentrations of ILs modified $CsPbBr_3$ films. The Shapiro–Wilk test was used to test normality of the distribution ($p > 0.05$) by using 40 individual devices of each type.

Conclusions

In this work, we have identified DTPT as dual-functional IL for both effective passivation of surficial/interfacial defects of the inorganic $CsPbBr_3$ perovskite phase, and effective suppression of the nucleation of impurity phases. Such synergistic effects enable large-area vapour deposition of low-defect and phase pure $CsPbBr_3$ films, and thus effectively mitigate the infamous high-defect problem of vapour deposited perovskite films.

The highly improved material quality owing to DTPT treatment is fundamental to achieving the highest efficiencies even without the use of expensive organic hole-transfer layer and precious metal electrode. Over 14% improvement of the PCE (9.83% to the highest 11.21%) was achieved on usual laboratory cells (0.04 cm^2), and more encouragingly, an average efficiency of 9.18% was also realized for large-area (1 cm^2) PSC cells. In addition, the DTPT treatment also helps improve the environmental stability of devices because of its remarkable hydrophobicity, so that exposed devices could maintain 91% of its initial efficiency after being placed in air with a relative humidity about 55% for 100 days.

The current effort towards a much-simplified photovoltaic architecture and successful vapour deposition of low-defect inorganic perovskite films provide a significant step forward for low-cost production of inorganic perovskite solar cells with an established manufacturing facility.

Author contributions

G. X. and G. S. provided facilities, funding and supervised the overall research work. R. G. and C. L. designed and conducted

the experiments, analysis and characterization. J. X. provided support in simulation and discussion. C. L. and H. G. provided optical characterization and analysis. Y. Z. participated in the preparation of $CsPbBr_3$ films and devices. X. M. and Z. W. provided SEM images. J. L. and Y. D. participated in the debugging and maintenance of the instrument. C. L. and Y. S. provided with mechanism analysis and discussion. All authors discussed the results and commented on the manuscript.

Conflicts of interest

There are no conflicts to declare.

Acknowledgements

The work is supported by the National Natural Science Foundation of China (no. 51602290), The Key R&D and Promotion Project of Henan Province (212102210600), Science and Technology Development Fund, Macao SAR (file no. FDCT-0044/2020/A1, FDCT-014/2017/AMJ), UM's Research Fund (file no. MYRG2018-00148-IAPME, MYRG2020-00151-IAPME), Natural Science Foundation of Guangdong Province, China (2019A1515012186), Guangdong-Hong Kong-Macao Joint Laboratory of Optoelectronic and Magnetic Functional Materials (2019B121205002), and Shenzhen-Hong Kong-Macao Science and Technology Innovation Project (Category C) (SGDX2020110309360100).

Notes and references

1 A. Kojima, K. Teshima, Y. Shirai and T. Miyasaka, *J. Am. Chem. Soc.*, 2009, **131**, 6050–6051.
2 National Renewable Energy Laboratory (NREL), 2021, **https://www.nrel.gov/pv/cell-efficiency.html**.
3 M. Shahiduzzaman, E. Y. Muslih, A. K. M. Hasan, L. Wang, S. Fukaya, M. Nakano, M. Karakawa, K. Takahashi, M. Akhtaruzzaman, J.-M. Nunzi and T. Taima, *Chem. Eng. J.*, 2021, **411**, 128461.
4 G. Zhang, P. Xie, Z. Huang, Z. Yang, Z. Pan, Y. Fang, H. Rao and X. Zhong, *Adv. Funct. Mater.*, 2021, **31**, 2011187.
5 J. Liang, C. Wang, Y. Wang, Z. Xu, Z. Lu, Y. Ma, H. Zhu, Y. Hu, C. Xiao, X. Yi, G. Zhu, H. Lv, L. Ma, T. Chen, Z. Tie, Z. Jin and J. Liu, *J. Am. Chem. Soc.*, 2016, **138**, 15829–15832.
6 J. Duan, Y. Zhao, X. Yang, Y. Wang, B. He and Q. Tang, *Adv. Energy Mater.*, 2018, **8**, 1802346.
7 Q. Zhou, J. Duan, J. Du, Q. Guo, Q. Zhang, X. Yang, Y. Duan and Q. Tang, *Adv. Sci.*, 2021, **8**, 2101418.
8 G. Tong, T. Chen, H. Li, L. Qiu, Z. Liu, Y. Dang, W. Song, L. K. Ono, Y. Jiang and Y. Qi, *Nano Energy*, 2019, **65**, 104015.
9 M. Liu, M. B. Johnston and H. J. Snaith, *Nature*, 2013, **501**, 395–398.
10 G. Tong, H. Li, G. Li, T. Zhang, C. Li, L. Yu, J. Xu, Y. Jiang, Y. Shi and K. Chen, *Nano Energy*, 2018, **48**, 536–542.
11 Y. Zhao, J. Duan, Y. Wang, X. Yang and Q. Tang, *Nano Energy*, 2020, **67**, 104286.
12 C. Liang, H. Gu, Y. Xia, Z. Wang, X. Liu, J. Xia, S. Zuo, Y. Hu, X. Gao, W. Hui, L. Chao, T. Niu, M. Fang, H. Lu, H. Dong, H. Yu, S. Chen, X. Ran, L. Song, B. Li, J. Zhang, Y. Peng, G. Shao, J. Wang, Y. Chen, G. Xing and W. Huang, *Nat. Energy*, 2020, **6**, 38–45.
13 T. Niu, L. Chao, W. Gao, C. Ran, L. Song, Y. Chen, L. Fu and W. Huang, *ACS Energy Lett.*, 2021, **6**, 1453–1479.
14 S. Bai, P. Da, C. Li, Z. Wang, Z. Yuan, F. Fu, M. Kawecki, X. Liu, N. Sakai, J. T. Wang, S. Huettner, S. Buecheler, M. Fahlman, F. Gao and H. J. Snaith, *Nature*, 2019, **571**, 245–250.
15 Y.-H. Lin, N. Sakai, P. Da, J. Wu, H. C. Sansom, A. J. Ramadan, S. Mahesh, J. Liu, R. D. J. Oliver, J. Lim, L. Aspitarte, K. Sharma, P. K. Madhu, A. B. Morales-Vilches, P. K. Nayak, S. Bai, F. Gao, C. R. M. Grovenor, M. B. Johnston, J. G. Labram, J. R. Durrant, J. M. Ball, B. Wenger, B. Stannowski and H. J. Snaith, *Science*, 2020, **369**, 96–102.
16 J. Xia, C. Liang, S. Mei, H. Gu, B. He, Z. Zhang, T. Liu, K. Wang, S. Wang, S. Chen, Y. Cai and G. Xing, *J. Mater. Chem. A*, 2021, **9**, 2919–2927.
17 A. Wang, X. Deng, J. Wang, S. Wang, X. Niu, F. Hao and L. Ding, *Nano Energy*, 2021, **81**, 105631.
18 C. Altinkaya, E. Aydin, E. Ugur, F. H. Isikgor, A. S. Subbiah, M. D. Bastiani, J. Liu, A. Babayigit, T. G. Allen, F. Laquai, A. Yildiz and S. D. Wolf, *Adv. Mater.*, 2021, **33**, 2005504.
19 Q. Jiang, L. Zhang, H. Wang, X. Yang, J. Meng, H. Liu, Z. Yin, J. Wu, X. Zhang and J. You, *Nat. Energy*, 2016, **2**, 16177.
20 W. Ke, G. Fang, Q. Liu, L. Xiong, P. Qin, H. Tao, J. Wang, H. Lei, Bo. Li, J. Wan, G. Yang and Y. Yan, *J. Am. Chem. Soc.*, 2015, **137**, 6730–6733.
21 Y. Zhang, X. Liu, P. Li, Y. Duan, X. Hu, F. Li and Y. Song, *Nano Energy*, 2019, **56**, 733–740.
22 K. C. Tang, P. You and F. Yan, *Sol. RRL*, 2018, **2**, 1800075.
23 Y. Zhao, Q. Deng, R. Guo, Z. Wu, Y. Li, Y. Duan, Y. Shen, W. Zhang and G. Shao, *ACS Appl. Mater. Interfaces*, 2020, **12**, 54904–54915.
24 X. Wang, Y. Wang, Y. Chen, X. Liu and Y. Zhao, *Adv. Mater.*, 2021, **33**, 2103688.
25 D. Yang, X. Li, W. Zhou, S. Zhang, C. Meng, Y. Wu, Y. Wang and H. Zeng, *Adv. Mater.*, 2019, **31**, 1900767.
26 X. Li, Y. Wu, S. Zhang, B. Cai, Y. Gu, J. Song and H. Zeng, *Adv. Funct. Mater.*, 2016, **26**, 2435–2445.
27 Y.-H. Kim, J. S. Kim and T.-W. Lee, *Adv. Mater.*, 2019, **31**, 1804595.
28 W. Xu, Q. Hu, S. Bai, C. Bao, Y. Miao, Z. Yuan, T. Borzda, A. J. Barker, E. Tyukalova, Z. Hu, M. Kawecki, H. Wang, Z. Yan, X. Liu, X. Shi, K. Uvdal, M. Fahlman, W. Zhang, M. Duchamp, J.-M. Liu, A. Petrozza, J. Wang, L.-M. Liu, W. Huang and F. Gao, *Nat. Photonics*, 2019, **13**, 418–424.
29 S. Yun, X. Zhou, J. Even and A. Hagfeldt, *Angew. Chem., Int. Ed.*, 2017, **56**, 15806–15817.
30 H. Huang, M. I. Bodnarchuk, S. V. Kershaw, M. V. Kovalenko and A. L. Rogach, *ACS Energy Lett.*, 2017, **2**, 2071–2083.
31 X. Zheng, Y. Hou, C. Bao, J. Yin, F. Yuan, Z. Huang, K. Song, J. Liu, J. Troughton, N. Gasparini, C. Zhou, Y. Lin, D.-J. Xue, B. Chen, A. K. Johnston, N. Wei, M. N. Hedhili, M. Wei, A. Y. Alsalloum, P. Maity, B. Turedi, C. Yang, D. Baran, T. D. Anthopoulos, Y. Han, Z.-H. Lu, O. F. Mohammed,

F. Gao, E. H. Sargent and O. M. Bakr, *Nat. Energy*, 2020, **5**, 131–140.

32 S. Tombe, G. Adam, H. Heilbrunner, D. H. Apaydin, C. Ulbricht, N. S. Sariciftci, C. J. Arendse, E. Iwuoha and M. C. Scharber, *J. Mater. Chem. C*, 2017, **5**, 1714–1723.

33 S. Sun, T. Salim, N. Mathews, M. Duchamp, C. Boothroyd, G. Xing, T. C. Sum and Y. M. Lam, *Energy Environ. Sci.*, 2014, **7**, 399–407.

34 G. Mannino, I. Deretzis, E. Smecca, A. La Magna, A. Alberti, D. Ceratti and D. Cahen, *J. Phys. Chem. Lett.*, 2020, **11**, 2490–2496.

35 Y. Wei, Y. Zhao, C. Liu, Z. Wang, F. Jiang, Y. Liu, Q. Zhao, D. Yu and M. Hong, *Adv. Funct. Mater.*, 2021, **31**, 2106386.

36 D. Shi, V. Adinolfi, R. Comin, M. Yuan, E. Alarousu, A. Buin, Y. Chen, S. Hoogland, A. Rothenberger and K. Katsiev, *Science*, 2015, **347**, 519–522.

37 J. Guo, Z. Shi, J. Xia, K. Wang, Q. Wei, C. Liang, D. Zhao, Z. Zhang, S. Chen, T. Liu, S. Mei, W. Hui, G. Hong, Y. Chen and G. Xing, *Small*, 2021, 2100560.

38 M. De Bastiani, I. Dursun, Y. Zhang, B. A. Alshankiti, X.-H. Miao, J. Yin, E. Yengel, E. Alarousu, B. Turedi, J. M. Almutlaq, M. I. Saidaminov, S. Mitra, I. Gereige, A. AlSaggaf, Y. Zhu, Y. Han, I. S. Roqan, J.-L. Bredas, O. F. Mohammed and O. M. Bakr, *Chem. Mater.*, 2017, **29**, 7108–7113.

39 G. Xing, N. Mathews, S. S. Lim, N. Yantara, X. Liu, D. Sabba, M. Gratzel, S. Mhaisalkar and T. C. Sum, *Nat. Mater.*, 2014, **13**, 476–480.

40 C. Liang, D. Zhao, P. Li, B. Wu, H. Gu, J. Zhang, T. W. Goh, S. Chen, Y. Chen, Z. Sha, G. Shao, T. C. Sum and G. Xing, *Nano Energy*, 2019, **59**, 721–729.

41 S. Wang, Z. Li, Y. Zhang, X. Liu, J. Han, X. Li, Z. Liu, S. Frank Liu and W. C. H. Choy, *Adv. Funct. Mater.*, 2019, **29**, 1900417.

42 C. Liang, K. M. M. Salim, P. Li, Z. Wang, T. M. Koh, H. Gu, B. Wu, J. Xia, Z. Zhang, K. Wang, T. Liu, Q. Wei, S. Wang, Y. Tang, G. Shao, Y. Song, N. Mathews and G. Xing, *J. Mater. Chem. A*, 2020, **8**, 5874–5881.

43 N. Yarita, H. Tahara, T. Ihara, T. Kawawaki, R. Sato, M. Saruyama, T. Teranishi and Y. Kanemitsu, *J. Phys. Chem. Lett.*, 2017, **8**, 1413–1418.

44 Q. Zhou, J. Duan, X. Yang, Y. Duan and Q. Tang, *Angew. Chem., Int. Ed.*, 2020, **59**, 21997–22001.

45 X. Zhu, M. Du, J. Feng, H. Wang, Z. Xu, L. Wang, S. Zuo, C. Wang, Z. Wang, C. Zhang, X. Ren, S. Priya, D. Yang and S. F. Liu, *Angew. Chem., Int. Ed.*, 2021, **60**, 4238–4244.

46 W. Zhang, X. Liu, B. He, Z. Gong, J. Zhu, Y. Ding, H. Chen and Q. Tang, *ACS Appl. Mater. Interfaces*, 2020, **12**, 4540–4548.

47 G. Shao, *Energy Environ. Mater.*, 2021, **4**, 273–276.

48 G. Tong, T. Chen, H. Li, W. Song, Y. Chang, J. Liu, L. Yu, J. Xu, Y. Qi and Y. Jiang, *Sol. RRL*, 2019, **3**, 1900030.

49 N. Ahn, K. Kwak, M. S. Jang, H. Yoon, B. Y. Lee, J. K. Lee, P. V. Pikhitsa, J. Byun and M. Choi, *Nat. Commun.*, 2016, **7**, 13422.

50 Q. Wang, B. Chen, Y. Liu, Y. Deng, Y. Bai, Q. Dong and J. Huang, *Energy Environ. Sci.*, 2017, **10**, 516–522.

51 X. Deng, L. Xie, S. Wang, C. Li, A. Wang, Y. Yuan, Z. Cao, T. Li, L. Ding and F. Hao, *Chem. Eng. J.*, 2020, **398**, 125594.

52 Y. Li, J. Duan, H. Yuan, Y. Zhao, B. He and Q. Tang, *Sol. RRL*, 2018, **2**, 1800164.

53 G. Greczynski and L. Hultman, *Angew. Chem., Int. Ed.*, 2020, **132**, 5034–5038.

54 G. Greczynski and L. Hultman, *Appl. Surf. Sci.*, 2018, **451**, 99–103.

55 H. J. Monkhorst and J. D. Pack, *Phys. Rev. B: Solid State*, 1976, **13**, 5188–5192.

